

The Application of Lobe Dynamics to Barotropic Rossby-Wave Breaking

Tieh-Yong Koh and R. Alan Plumb

Massachusetts Institute of Technology, Cambridge, MA 02139.

Abstract

We applied the methods of lobe dynamics to the problem of transport across the edge of a barotropic vortex-patch. The model used captures the essential dynamics of filament-shedding in the wintertime stratospheric polar vortex. Two approaches were adopted for the problem: (1) the dominant periodic component of the vortical flow was identified and conventional lobe dynamics methods for periodic dynamical systems were applied to it; (2) the full aperiodic, dynamically consistent flow was retained and a modified brand of lobe dynamics was used to quantify the transport. Our results show that in the periodic case, much reversible transport occurs across the lobe dynamical boundary due to overlapping intruding and extruding lobes. In the aperiodic case, a small amount of intrusion was noted, contrary to the well-established fact that potential vorticity shedding in barotropic vortices is uniquely outwards. In our discussion, we argue that while lobe dynamics provides a rigorous framework for quantifying transport across the lobe dynamical boundary, this boundary may not be appropriate for quantifying transport across internal transport barriers, such as the stratospheric polar vortex edge.

Contents

1	Introduction	3
2	Model Description	4
3	First Approach: Periodic Flow	6
4	Second Approach: Aperiodic Flow	8
5	Discussion	10
5.1	Lobe Dynamics in the Periodic Case	10
5.2	Lobe Dynamics in the Aperiodic Case	11
5.3	Lobe Dynamical Transport vs. Vortex Edge Transport	11
5.4	Asymmetric PV Transport across the Vortex Edge	12
6	Conclusions	13
	Acknowledgements	13
	Appendix	14
A.	Location of the Hyperbolic Trajectory	14
B.	Some Mathematical Details	15
C.	Time-symmetric node advection scheme	17
	References	17
	Tables	21
	Figures	22

1 Introduction

The particular atmospheric problem of interest in this paper is the issue of tracer transport across the edge of the polar vortex in the lower winter stratosphere. This is an important problem in its own right : amongst other things, transport across the vortex edge is thought to have a significant influence on the ozone chemistry both within and outside the vortex^[1]. It also serves as a paradigm for a wide range of geophysical fluid dynamical problems, e.g. leakiness of the stratospheric “tropical pipe”^[2], stratosphere-troposphere exchange by tropopause-folding^[3], lower tropospheric water vapour transport^[4], and cross-stream mixing in the ocean^{[5],[6],[7],[8]}. In many Lagrangian-chaotic flows, a well-mixed zone flanked by internal transport “barriers” is formed through the stretching and folding associated with the transport itself^[9]. The transport barriers are identified by sharp tracer and potential vorticity gradients. In the winter stratosphere, the polar vortex edge is such a barrier, and cross-edge transport is effected by Rossby-wave breaking^[10]. Filaments of polar vortex material are ejected into middle latitudes, where they eventually dissipate^[11]. Entrainment of mid-latitude air into the vortex has also been observed^[12], but it is much less frequent.

Methods have been devised to quantify such transport, using data from atmospheric observations^{[1],[11],[12],[13]} or from models^{[14],[15],[16]}. A wide range of values has been obtained from these studies, because different definitions were adopted for the boundaries across which the transport was measured. Indeed, Sobel et al. (1997)^[15] argued that making the appropriate choice of boundary across which to measure transport is the crux of the transport calculation: the computed mass fluxes may be very sensitive to that choice.

Set in the above context, we wish to investigate whether lobe dynamics provides a useful framework for measuring transport across the vortex edge, using the vortex-patch model of Polvani and Plumb (1992)^[17]. Lobe dynamics has been employed to quantify transport in certain modeled^{[5],[6]} and observed^{[7],[18]} oceanic flows. Its distinguishing feature in such applications is the definition of a boundary, based solely on flow kinematics, across which transport is measured. In all these cited work, lobe dynamics yields rigorous and precise quantification of transport, hence providing much motivation for applying it to the stratospheric polar vortex problem. Recently, Bowman (1999)^[19] even revealed the presence of stable and unstable manifolds in the stratosphere, following the practical approach of Miller et al. (1997)^[6].

With regards to theory, lobe dynamics pertaining to periodic dynamical systems has a long tradition in the literature. We merely cite two recent work here: Ottino (1989)^[9] introduces the subject with an emphasis on applications to fluid mixing and transport; and Wiggins (1992)^[20] takes on the subject with a rigorous mathematical approach. References to older literature can be found in both these recent work.

The lobe dynamics for aperiodic dynamical systems have also been investigated before in the literature, but is less firmly established than for periodic systems. Again citing only recent examples, Malhotra and Wiggins (1998)^[21] extended the infinite-time formulation of lobe dynamics to aperiodic flows and applied the theory to a range

of kinematic flows with small parameters. Subsequently, the theory was successfully applied to computational^[8] and observed oceanic flows^[18]. On the other hand, Miller et al. (1997)^[6] examined lobe dynamical transport over a finite time interval across an aperiodic meandering barotropic jet on a β -plane. Their work was followed by Haller and Poje (1998)^[22], where finite-time lobe dynamics theory was formulated and used to study cross-stream mixing effected by Gulf Stream Rings. The approach of Malhotra and Wiggins (1998) and those of Miller et al. (1997) and Haller and Poje (1998) are related but different as the latter two emphasized finite-time behaviour of aperiodic systems.

In this paper, lobe dynamics is applied to the model stratospheric polar vortex via two approaches. In the first approach, we relied on the fact that the modeled flow is close to periodic after an initial adjustment period. This allows us to apply lobe dynamics to the dominant periodic component of the flow, making use of well-established theory. The objective here is to evaluate how well the existing technique performs in a kinematic flow bearing the cat’s eye feature frequently encountered in wintertime stratospheric flow.

In the second approach, we retained the full aperiodic dynamically consistent flow. But we employed an ad-hoc modification of the aperiodic lobe dynamics theory, as we found that none of the existing theory that we are aware of^{[21],[22]} suits our purpose. The goal is to assess whether transport across the lobe dynamical boundary is an appropriate characterization of the transport across the vortex edge.

We delay our discussion until after the results of both approaches are presented, and we shall note the shortcomings and merits of the lobe dynamical view of transport across the stratospheric polar vortex edge.

2 Model Description

The object of investigation is a barotropic vortex-patch model derived from the quasi-geostrophic shallow-water model of Polvani and Plumb (1992)^[17]. This model is able to capture the essence of the dynamics associated with the stratospheric polar vortex, yet its simplicity renders its transport characteristics self-evident. In the model, the transport barrier is simply the jump in potential vorticity at the vortex edge, and so transport across it can be quantified by performing *surgery* on the contour demarcating the discontinuity, in the manner described in Dritschel (1988)^[23]. Having such a natural “boundary” makes the model ideal as a test bed for other transport-measuring schemes. In the literature, barotropic models have also been used before to study the dynamics of the stratospheric polar vortex (see e.g. Juckes and McIntyre 1987^[24]).

A brief model description follows next. For further details, the reader is referred to Polvani and Plumb (1992)^[17]. The model is based on inviscid quasi-geostrophic shallow-water dynamics on an f -plane, and uses the Contour Dynamics with Surgery (CDS) algorithm of Dritschel (1988)^[23]. The mean depth is D and the system is forced by time-dependent bottom topography h . The system is governed by the conservation of potential vorticity (PV), as follows :

$$\left(\frac{\partial}{\partial t} - \frac{\partial\psi}{\partial y}\frac{\partial}{\partial x} + \frac{\partial\psi}{\partial x}\frac{\partial}{\partial y}\right)\mathcal{Q} = 0 \quad (1)$$

$$\mathcal{Q} = f_0 + \nabla^2\psi - \gamma^2\psi + f_0\frac{h}{D} \quad (2)$$

where \mathcal{Q} is the potential vorticity, f_0 is the constant planetary vorticity, ψ is the streamfunction of the geostrophic flow, and γ is the inverse Rossby deformation radius (i.e. f_0/\sqrt{gD}).

Since lobe dynamics is formulated for non-divergent flows, we let $\gamma \rightarrow 0$, so that the flow is in the barotropic limit. The model is initialized at Day 0 (where a day is defined as $4\pi/f_0$) as a circular PV vortex-patch embedded in a uniform background of lower PV. That is,

$$\mathcal{Q} = \begin{cases} \mathcal{Q}_i & \text{if } r < r_0 \\ \mathcal{Q}_o & \text{otherwise} \end{cases}$$

Since the wind speed increases without limit as radial distance increases, we shall restrict our attention to the domain within $4r_0$ from the origin. The air in this region is isolated from the rest of the f-plane from Day 0 to Day 20, as we confirmed with the advection of a material contour initially at radius $4r_0$.

The topographic forcing, in polar coordinates (r, θ) about the origin, takes the form :

$$h(r, \theta, t) = DH_0(1 - e^{-t/\tau})J_1(\kappa r) \cos \theta$$

where $J_1(\kappa r)$ is the 1st order Bessel function of the first kind and H_0 is a dimensionless parameter that governs the strength of the forcing. The forcing is aperiodic and its time-dependence dies away for $t \gg \tau$ as the topography approaches a constant height. Figure 1 shows the spatial form of the forcing.

The following set of parameters is used for all work in this paper: $\mathcal{Q}_i = 1.3f_0$, $\mathcal{Q}_o = 0.9f_0$, $\kappa = 1.6/r_0$, $\tau = 2.5\text{days}$, $H_0 = 0.17$. The above choice of values follows Polvani and Plumb (1992)^[17]. If we take r_0 as 3000km and equate a model day to a real day, these parameter values yield wind velocities that are roughly consistent with observations in the Northern hemisphere mid-latitude lower stratosphere. Our comparison with the stratosphere should be taken with caution however, as the model is idealized. But for convenience, we shall sometimes refer to the origin as the “pole” and the region outside $4r_0$ as the “tropics”.

We have chosen a slightly supercritical value for H_0 so as to get the PV vortex breaking but not too violently, since we do not wish to complicate the lobe dynamics in our preliminary application. Please refer to Polvani and Plumb(1992)^[17] for details on the different dynamical regimes for this model flow. Incidentally, the weak Rossby-wave breaking in the polar vortex is well-surveyed in the literature (see e.g. Waugh et al. (1994)^[11], Plumb et al.(1994)^[12]) so that we have a reasonable basis to compare our results to.

The following CDS parameter values are employed : $\mu = 0.1$, $\delta = r_0/800$, $\delta t = 1/20\text{day}$, where μ is a measure of the node density on contours, δ is the smallest separation between contour segments before they merge, and δt is the time step used in the computation^[23]. An increase in μ or a decrease in δ or δt does not significantly alter the subsequent observed evolution of PV.

From a single prognostic run, all contour node positions are saved at every time step. The saved PV contours represent compressed high resolution wind data, through the invertibility principle (equation (2)). Advection of particles and material contours in subsequent diagnostic runs uses winds at the particle and contour node positions, inverted from the PV contours at every time step. Consistency between forward and backward advection of the same particle or contour is ensured through the following features:

- a common set of PV contours (wind data) for both forward and backward runs;
- a 4th order “Runge-Kutta-like” node advection scheme that respects time symmetry (c.f. Appendix C);
- higher node density ($\mu = 0.05$) than in the prognostic run;
- switching off surgery on the passive contours ($\delta = 0$).

Such consistency is important since the diagnostic runs essentially involve forward-backward-forward and backward-forward-backward advection sequences. The evolution of the PV and streamfunction are depicted in Figure 2.

As mentioned, the transport barrier in this model is simply the PV jump across the vortex edge, the vortex being defined as the largest contiguous patch of high vorticity after filaments have been cut off from it by contour surgery. From the discontinuous reduction of the vortex area, we measured that the filament-shedding events after Day 12.5 and Day 17.5 constitute outward transport of high-PV material by amounts of $0.136r_0^2$ and $0.477r_0^2$ respectively.

3 First Approach: Periodic Flow

Inspection of the streamlines in Figure 2 shows that from Day 2.5 onwards, a dominant period of 7.5 days has evolved, as the forcing becomes increasingly steady. So, we extracted the dominant component of the flow that repeats every 7.5 days. In doing this, one may formally perform a discrete Fourier transform of the flow from Day 2.5 to Day 17.5 and pick out every second spike in the frequency spectrum, starting from the gravest end. The resulting flow is then identical to an equal-weighting composite constructed from the aperiodic flow during the two intervals [Day 2.5, Day 10] and [Day 10, Day 17.5]. Figure 3 shows the composite flow, where the cycle starts with Day 2.5, for ease of comparison with Figure 2. Because equation (1) is nonlinear, potential vorticity is not conserved in this composite flow cycle. It is interesting to note that this approach to obtaining periodic flows out of aperiodic flows differs from

the approach adopted in Miller et al. (1997)^[6]. In that paper, the authors truncated the aperiodic flow field after one single dominant periodic cycle and repeated the entire flow field for that time interval indefinitely into the future.

To see the lobe dynamics of the composite flow, we followed Miller et al. (1997)^[6] by using the hyperbolic stagnation point of the time-averaged flow as an estimate of the location of the hyperbolic trajectory. In this, we assumed the flow could be decomposed into a large steady component and a small periodic perturbation. Next, a small circular passive tracer contour was constructed around that location on Day 2.5. It was separately advected forwards and backwards in time for one period so that it would collapse onto the unstable and stable manifolds respectively, thus locating them. Then, the stable manifold was phase-shifted forwards in time by two periods to intersect the unstable manifold and identify the hyperbolic trajectory on Day 10 and hence also on Day 2.5 and Day 17.5 as the flow is periodic. Finally, sections of the collapsed contours around the manifolds spanning across the hyperbolic trajectory were again advected forwards from Day 2.5 and backwards from Day 17.5, to locate respectively the unstable and stable manifolds and hyperbolic trajectory with higher precision.

The practice of allowing passive tracers to collapse onto manifolds, thereby revealing the location of stable and unstable manifolds and the hyperbolic trajectory is rather common in the literature^{[6],[21]}. What is different here is the numerical technique we use: Dritschel’s algorithm for contour advection is applied to the passive tracer contours. The method is essentially the same as Contour Advection with Surgery (CAS) discussed in Waugh and Plumb (1994)^[25], except that surgery was not performed on the contours in order to maintain an unbroken trace of the manifolds. In brief, the tracer contours are represented by nodes that are passively advected by the wind field, and they are renoded constantly to ensure good resolution of fine-scale features.

The lobes identified in this manner are shown in Figure 4. The intersection points between the stable and unstable manifolds, that are connected to the hyperbolic trajectory by unintersected segments of the manifolds, are known as the primary intersection points (PIP). They are labeled as B_n ’s in the figure. Note that the position of B_3 on Day 10 is identical to that of B_1 on Day 2.5, as the cycle repeats every 7.5 days. Given a reference PIP, say B_n , the lobe dynamical boundary is defined as the union of the segment of the unstable manifold between B_n and the hyperbolic trajectory, and the segment of the stable manifold between B_n and the hyperbolic trajectory. It is indicated by the thick line in the figure. The reference PIP that determines the lobe dynamical boundary, B_n , is redefined to the PIP upstream, $B(n+1)$, when the stable manifold between B_n and $B(n+1)$ has shortened to less than Σ .

The above definition for the lobe dynamical boundary has the advantage of being stationary in Poincare sections. In fact, it is the transport boundary conventionally adopted in Poincare sections (c.f. Section 3.3.1 of Malhotra and Wiggins (1998)^[21]). Traditional Poincare-section analyses of periodic systems implicitly redefine the reference PIP to the second PIP upstream at the moment that each Poincare section is taken. But when the system is considered in continuous time, the timing of the

redefinition of the reference PIP acquires an added freedom within a period. The choice of Σ affects only this timing and not the amount of transport, as the latter is dependent only on lobe areas. Since it is not an objective of this paper to address the timing of intrusion and extrusion events, a reasonably small value of $\Sigma = 0.3r_0$ is conveniently assumed.

Table I shows the transport across the lobe dynamical boundary. It is a well-known theorem (see e.g. Ottino (1989)^[9]) that in a periodic flow, there exists an infinite number of lobes in any tangle between the unstable and stable manifolds, and they all have equal areas. Our numerical computation show that the intruding and extruding lobes, Li and Le, have roughly equal but not identical area. The error values for Li and Le in Table I refer to the uncertainty due to the incomplete collapse of the computed passive contours onto the manifolds. Uncertainties from other sources, e.g. the discrete representation of contours and the finite resolution in the saved PV field, are not estimated. Thus, the discrepancy in area between Li and Le is attributed to the accumulation of these unaccounted errors during contour advection, which is substantial because of the exponential stretching in the Lagrangian-chaotic flow.

Therefore, we estimate that the true lobe dynamical transport to be $(0.67 \pm 0.05)r_0^2$ in each direction. About half of the cancelation between inward and outward transport comes from the reversible migration of the fluid parcel defined by the overlap O between Li and Le (see Figure 4). Contrast this with the *exclusive* outward transport of $0.613r_0^2$ measured across the vortex edge by the contour surgery algorithm.

4 Second Approach: Aperiodic Flow

In this section, we apply lobe dynamics to the full aperiodic vortex flow shown in Figure 2. This is arguably the more relevant approach, since we do not expect the wintertime stratospheric flow to be often dominated by a large periodic component. Additionally, the lobe dynamical transport in the periodic component flow revealed in the previous section is quite different from what we might expect from performing contour surgery on the simple model vortex. We are interested in the transport from Day 0 to Day 17.5. From Day 17.5 to Day 20, the roll-up of a filament signifies the possible existence of a secondary hyperbolic point in the flow, and hence for the sake of simplicity, that time interval is excluded. The initial adjustment period, Day 0 to Day 2.5, is included to introduce a large aperiodic component to the case study, as we do not expect the aperiodicity in real stratospheric flows to have small amplitude.

Regarding the lobe dynamics of aperiodic systems, as pointed out in the Introduction, we are currently aware of two different approaches in the literature. In Malhotra and Wiggins (1998)^[21], the hyperbolic trajectory is the particle trajectory to which particle trajectories on the stable and unstable manifolds converge as time approaches positive and negative infinity respectively, just as in periodic lobe dynamics theory. In that paper, the theory was applied to steady or periodic flows which are disturbed by an aperiodic component with an ϵ -amplitude parameter, where hyperbolic trajectories were proven to exist. And in more recent work, the theory has been applied to a 3-layer double-gyre quasi-geostrophic ocean model^[8], as well as real oceanic flows

in Monterey Bay, California^[18]. However, the theoretical conditions for the existence of hyperbolic trajectories in an aperiodic flow of a general nature, such as our model flow from Day 0 to Day 17.5, has not been established.

Haller and Poje (1998)^[22] formulated a theory of finite-time lobe dynamics. For a given finite time interval where a hyperbolic stagnation point exists in the streamfunction, the authors show rigorously that a hyperbolic trajectory, and its associated stable and unstable manifolds, exist if the flow satisfies certain specified constraints. The manifolds and the hyperbolic trajectory identified in this manner are not unique, but their identity converges exponentially with the length of the finite time interval. However, in our model, the hyperbolic stagnation point in the streamfunction is non-existent around Day 12.5. To use the method, it appears that one has to divide the associated lobe dynamics from Day 0 to Day 17.5 into two separate episodes, each with its own hyperbolic trajectory. But note that the separation of the filament from the vortex after Day 12.5 in Figure 2 is not due to the stagnation point vanishing, but is brought about by the contour surgery algorithm. When a smaller CDS parameter δ is specified, the filament continues to stretch exponentially, even though the stagnation point vanishes around Day 12.5. This seems to indicate that the breaking event ought to be associated with a single hyperbolic trajectory through Day 12.5. Additionally, from a conceptual standpoint, lobe dynamical structures, being inherently Lagrangian in nature, should have an uninterrupted identity, even when Eulerian structures are transitory during the period of interest. Moreover, hyperbolic stagnation points may vanish in one frame, while persisting in another. The reason is that the topology of Eulerian flow depends on the frame of reference. No single frame can be appropriate for all circumstances, and it is unsure if there always exists an appropriate frame (e.g. when a given flow has a spectrum of dispersive waves). Therefore, our model is not accessible to this approach, at least without a clearer idea of what the appropriate frame of reference is.

Although the above two approaches to aperiodic lobe dynamics are different in theoretical details, they employ the same principles in practice – the hyperbolic trajectory is a particle trajectory about which there is strong exponential deformation of the fluid substance, and that this deformation lasts long enough for the stable and unstable manifolds to be located by the exponential approach of tracers lines. So, while both theoretical approach are not suitable to our case study for their own reasons, the common gist of their implementation methods is still applicable.

For lack of a more appropriate approach, we therefore made the following ad-hoc modification to the theories of aperiodic lobe dynamics: for the hyperbolic trajectory, we select the particle about which there is the *greatest* exponential deformation of the fluid substance from Day 0 to Day 17.5. The details of how we locate this trajectory and how we measure the exponential deformation are relegated to Appendix A and B. Here, it suffices to note that the method is meant for finite-time applications, and is based on Lagrangian kinematics. The unstable manifold is located by the (incomplete) exponential collapse of a circular tracer contour of radius Δ around the hyperbolic trajectory in forward time starting from Day 0, using Dritschel’s contour advection algorithm without surgery^[23]. It may be thought of as the material line that straddles the hyperbolic trajectory and has the greatest increase in length from

Day 0 to Day 17.5. But such an interpretation is not essential to the practical implementation of the method. The stable manifold can be similarly located and interpreted, except in reverse time starting from Day 17.5. In our case, we used $\Delta = 0.2r_0$.

Figure 5 shows the lobe dynamics in the aperiodic vortex flow on Day 8.5 and subsequent times when a lobe extrusion or an intrusion occurs. The definition of the lobe dynamical boundary in the aperiodic case is the same as in the periodic case, following Malhotra and Wiggins (1998)^[21]. The lobe dynamical boundary (thick full line) separates an interior region (henceforth “LD-interior”) from an exterior region (henceforth “LD-exterior”). The alternating intrusion and extrusion of lobes, aptly called “turnstile transport”, is clearly seen in Figure 6. Note that the exchange mediated by lobes occurs directly between the vortex-edge region (the “subpolar” region) and the region of anticyclonic flow (the “subtropical” region). This transport is nonlocal, and so if the tracer field has a meridional gradient, the lobes will bring air parcels of disparate tracer mixing ratios together, enhancing the efficacy of subsequent mixing. Contrast this mechanism with diffusion which, by its local nature, mixes air parcels of only slightly different tracer mixing ratios in a continuous tracer distribution.

From Table II, the total outward transport measured by lobe dynamics from Day 0 to Day 17.5 is $(1.52 \pm 0.03)r_0^2$ while the total inward transport measured is $(0.110 \pm 0.001)r_0^2$, with the convenient choice of $\Sigma = \Delta = 0.2r_0$. This is much larger than the PV transport $0.613r_0^2$ measured by the contour surgery method. We can understand this as follows: the area of the LD-interior prior to any transport is $(4.32 \pm 0.04)r_0^2$, larger than the area πr_0^2 of the vortex on Day 0. This indicates that the LD-interior includes non-vortex air along its periphery. Consequently, much of the extruded air, which originates in the periphery of the LD-interior, has low PV and so does not contribute to PV transport.

Cancellation between inward and outward transport is only a small fraction ($7.2 \pm 0.2\%$) of the outward transport, because the intruding lobes are much smaller than the extruding lobes. Yet, the weak intrusions witnessed here are significant because their Lagrangian identities are distinct from the extrusions (i.e. the lobes do not overlap). They represent irreversible entrainment of LD-exterior air into the LD-interior from Day 0 to Day 17.5. Yet no low-PV entrainment into the vortex occurs, according to the contour surgery method.

5 Discussion

5.1 Lobe Dynamics in the Periodic Case

Because the theorem of equal lobe areas for periodic flows does not apply to the aperiodic flow, we may expect *a priori* that the lobe dynamical transport in any periodic flow component to be different from that in the full aperiodic flow. However, from theory alone, it is unclear how big these differences are. Contrasting Day 5.0 on Figure 4 and Day 12.5 on Figure 5, and Tables I and II, we see that the differences

are large, despite the two streamfunctions looking rather similar in Figures 2 and 3. In retrospect, the results affirm the well-known sensitivity of Lagrangian transport to Eulerian flow structures. More importantly, our results caution against taking the transport by the periodic flow component as the measure of transport in an aperiodic flow.

We also identified an interesting transport phenomenon in the periodic case. The instance of overlapping intruding and extruding lobes leading to reversible transport is dubbed as “pathological” in Malhotra and Wiggins (1998)^[21]. Thus, a rationalization for its occurrence appears in order. Now, in the periodic system, there must be as much fluid intruded as it is extruded. But the intruded fluid cannot really remain in the “interior”, because the transport is strongly asymmetric across the vortex edge in the aperiodic case, and the periodic flow is only slightly different from the aperiodic flow from Day 2.5 onwards. The most direct way to reconcile the two requirements is to have much of the intruded fluid extrude again before mixing can occur. To do this, the lobe dynamical boundary moves outwards from the vortex edge, thereby counting the bi-directional meridional stirring outside the vortex-patch as symmetric cross-boundary transport.

5.2 Lobe Dynamics in the Aperiodic Case

Figure 6 shows the close proximity between the lobe dynamical boundary and the vortex edge in the aperiodic flow. But note: the intruding lobe Li#1, composed entirely of low-PV air, is intruded into the LD-interior, but it is also evidently outside the vortex. The reason is that much of the PV filament previously wrapped around the vortex has been removed by contour surgery, leaving fragments (vis-a-vis the circles in Figure 6) that do not envelop Li#1. Hence, what is counted as an intrusion by lobe dynamics, is no more than peripheral stirring outside the vortex. Closer inspection of Figure 6 further reveals that Li#2 is composed entirely of high-PV air and is in the LD-exterior. Yet, Li#2 is clearly part of the vortex at this time and was never separated from it. The subsequent intrusion of Li#2 at Day 16.5 (see Figure 5) is then an illusion resulting from the categorical accounting procedure of lobe dynamics. As a result, the picture of transport according to lobe dynamics is qualitatively very different from that obtained by surgery of thin PV filaments. In the former, some intrusion has taken place, whilst in the latter, transport is exclusively outwards.

5.3 Lobe Dynamical Transport vs. Vortex Edge Transport

The distinction between the “turnstile” transport across the lobe dynamical boundary and that across the vortex edge is not merely one of semantics. First, continual stirring within the critical layer creates in the winter stratosphere, as in many similar flows, a clear distinction (such as in chemical composition) between air poleward of the vortex edge and the well-mixed air mass outside the edge. (In most cases, there will be a second barrier at the other side of critical layer. We eliminated that in our calculations simply by confining the PV gradient to a single contour.) Second, the

edge itself becomes a transport barrier, across which transport is much weaker than elsewhere (e.g. Sobel et al. (1997)^[15]). Thus, to the extent that one can usefully describe transport in such systems by a single measure, it is usually the transport across the barrier(s) that is the most critical measure.

While the outward transport across the lobe dynamical boundary is kinematically related to that across the vortex edge, the two will not usually be the same whenever the lobe dynamical boundary does not coincide with the edge. In the examples shown here, the two do not coincide. To some extent, this statement is trivial in the context of our model calculations, since the relative locations of the vortex edge and the hyperbolic trajectory are determined almost independently by the initial conditions and the bottom topography. In reality, it is stirring associated with the hyperbolic trajectory that creates the sharp vortex edge from continuous gradients (e.g. Juckes and McIntyre (1987)^[24]), so the two are not mutually independent. However, in a conservative flow, the location of the vortex edge depends on the past history of transport, while the lobe dynamical boundary is a function only of the kinematics during the period of interest. Even in a simple model such as that used here, there are certain parameter ranges in which a few events occur in which material is stripped off the vortex, following which transport across the edge ceases^[17], even though turnstile transport continues indefinitely within the critical layer. At least in the stratospheric context, the location of the vortex edge is also determined by nonconservative effects (in particular, radiative cooling acting on PV). Thus, we do not expect in general a precise relationship between the lobe dynamical boundary and the vortex edge.

5.4 Asymmetric PV Transport across the Vortex Edge

There is much observational evidence that extrusions of high-PV air occurs more frequently than intrusions of low-PV air in the stratospheric polar vortex^{[11],[12]}. Modeling studies come to essentially the same conclusion, although cases where intrusions dominate over extrusions could be contrived^[26]. For barotropic vortices such as the one in this paper, outward breaking of high-PV air seems to be the only form of cross-edge transport.

Although lobe dynamics may not provide a good framework for measuring cross vortex-edge transport, it does provide some insight into the phenomenon of asymmetric transport. In our case study, right from Day 0, the hyperbolic trajectory is located outside the PV vortex. Figure 7(a) is a schematic representation of the situation. Given this geometry, the high-PV filament extruded from the vortex must be nearer the unstable manifold than the low-PV air in lobe Li#1. Consequently the high-PV air undergoes strong exponential stretching and cascades to small scales before the low-PV air. It is reasonable, therefore, for it to be surgically removed before the low-PV air. (In the stratosphere, the downscale cascade of thin high PV filament would eventually be dissipated by molecular diffusion^[27].) The result is then a high-PV filament extruding and “mixing” into a low-PV environment, and not the converse.

We note in passing that if the hyperbolic trajectory is located inside a vortex

(Figure 7(b)), inward breaking will be the norm, such as the case with an interior critical line in Nakamura and Plumb (1994)^[26]. In the stratosphere, the bias for filament-shedding from the tropics into the surf zone can be explained in the same manner – the hyperbolic trajectory now lies polewards of the tropical easterly jet.

6 Conclusions

Previous work in the literature^{[9],[20],[21],[22]} have shown that lobe dynamics gives an engaging and mathematically precise framework for understanding transport in Lagrangian-chaotic flows. Intruding and extruding lobes have provided a systematic measure of transport in many oceanic flows^{[5],[6],[7],[8]}. In the winter stratosphere, the polar vortex edge is a throttle to tracer transport, and many methods have been devised to quantify the mass and tracer fluxes across it. However, the utility of lobe dynamics in this context was unknown. In this paper, we investigated this problem by adopting two approaches.

The periodic approach yielded material transport that is qualitatively very different from the PV transport measured by Dritschel’s contour advection algorithm. Equal quantities of air $(1.34 \pm 0.07)r_0^2$ are transported in both directions across the lobe dynamical boundary over two periods from Day 2.5 to Day 17.5, with about half of the quantity being reversible transport due to overlapping intruding and extruding lobes. The transport measured by the CDS algorithm was a total of $0.613r_0^2$ exclusively outwards from Day 0 to Day 17.5. The contrast highlights the fact that transport rates computed across the lobe dynamical boundary, which is located just outside the vortex edge, not only exaggerate the magnitude of transport, but also fail to capture its asymmetry.

In the aperiodic approach, there is an improvement in the representation of the asymmetry of transport – the total inward transport across the lobe-dynamical boundary is only $(7.2 \pm 0.2)\%$ of the total outward transport. However, the total outward transport of $(1.52 \pm 0.03)r_0^2$ from Day 0 to Day 17.5 is much larger than the transport of $0.613r_0^2$ measured by the CDS algorithm. This is because the interior defined by the lobe dynamical boundary initially includes much low-PV air which is extruded later on. The intruding lobes do not actually cross the transport barrier, vis-a-vis the edge of the vortex-patch. The underlying reasons are: (1) the categorical accounting procedure of lobe dynamics; and (2) the small but significant misalignment between the lobe dynamical boundary and the transport barrier.

Nevertheless, while not suitable as a quantitative theory of transport across the polar vortex edge, lobe dynamics does give some qualitative insight into the problem of asymmetric PV transport across the vortex edge.

Acknowledgements

The authors would like to thank Glenn Flierl for his suggestion of investigating the periodic case, Stephen Wiggins for an enlightening discussion on lobe dynamics, and

the two anonymous reviewers for their constructive criticisms which led to great improvements in this paper. Comments on the work and earlier versions of this paper by Gavin Esler, John Methven, and Adam Sobel have been most helpful too. This work was supported by the National Science Foundation, under grants ATM-9528471 and ATM-98190992.

Appendix

A. Location of the Hyperbolic Trajectory

We first located the locus of large instantaneous stretching from maps of $\det(M)$ at Day 0 and Day 17.5, where M is the velocity gradient tensor defined by equation (3) in Appendix B. The winds from which M was derived had been inverted on a regular grid of resolution $0.025r_0$ by $0.025r_0$. Negative $\det(M)$ indicates local strain dominating over local rotation, in which case $S = [-\det(M)]^{1/2}$ is the instantaneous rate of exponential stretching of small material elements, in certain time-dependent eigen-directions.

Note that $\det(M)$ is not a scalar – its value is not preserved under coordinate transformations. But the co-moving frame of the background flow is ideal for computing $\det(M)$ in our case, because the eigen-directions of $M(t)$ at the location of the hyperbolic trajectory varies the least with time in this frame (see e.g. Polvani et al. (1989)^[28]). In our model, the background flow is associated with the bottom topography and so $\det(M)$ is evaluated in the stationary frame.

As the mean rate of elongation of the PV contour from Day 0 to Day 17.5 was about 0.25/day, we chose $S_{th} = 0.25/\text{day}$ as the threshold beyond which S is considered significant. So, we advected contours demarcating the $\det(M) < -S_{th}^2$ region on Day 0 forwards in time, and other similar contours on Day 17.5 backwards in time. The intersection of regions enclosed by the forward-advected and backward-advected contours denote the fluid substance experiencing significant S on both Day 0 and Day 17.5. It was next verified that this set of fluid substance experienced significant S throughout Day 0 to Day 17.5.

On Day 10, this intersection set is least extended spatially. Visual inspection at this time shows that a subset of it, \mathcal{A} , lying near the hyperbolic stagnation point in the streamfunction, accumulates the most stretching both in forward advection from Day 0 to Day 10, and in backward advection from Day 17.5 to Day 10. Since the flow is incompressible, this implies that \mathcal{A} also accumulates the most stretching from Day 0 to Day 17.

Next, a coarse grid was set up over \mathcal{A} on Day 10 and a precise Lagrangian measure of exponential deformation – vis-a-vis the deformation exponent ξ defined by equation (5) in Appendix B – was calculated for all particles lying on the grid points. High values of ξ were aligned in cross-like formations, reminiscent of the homoclinic tangles around the hyperbolic trajectory (Figure 8). The calculation was repeated at finer and finer grids over the heart of the cross with the highest ξ . In the end, the particle X with the largest ξ on the finest grid was identified as the one closest to the hyperbolic

trajectory. The hyperbolic trajectory is taken here to be the particle in \mathcal{A} that has the largest ξ .

X was advected backwards to Day 0 and forwards to Day 17.5 to estimate the initial and final locations of the hyperbolic trajectory. To gauge the error in the estimates, a circular contour centered on X, with radius equal to half the finest grid resolution ($\sim 10^{-6}r_0$), was advected from Day 10 to Day 0 and from Day 10 to Day 17.5. On Day 0 and Day 17.5, these “error contours” lie within the judiciously chosen distance of $\Delta = 0.2r_0$ from X, so that tracer contours used to locate the stable and unstable manifolds do in fact envelop the hyperbolic trajectory.

Finally, note that the earlier calculation of $\det M$ in an appropriate Eulerian frame only serves to pick out the approximate location of the material set \mathcal{A} that has the highest cumulative exponential stretching. The subsequent identification of the hyperbolic trajectory within \mathcal{A} is not crucially dependent on this calculation (i.e. we can have a slightly different set \mathcal{A} and still be able to define the same hyperbolic trajectory). Hence, the method here is fundamentally based on Lagrangian kinematics and is independent of the Eulerian frame of reference.

B. Some Mathematical Details

The velocity gradient tensor M of 2D flows is given by Batchelor (1967)^[29] in cartesian coordinates (x, y) as:

$$M(t) \equiv \begin{bmatrix} \frac{\partial u}{\partial x} & \frac{\partial u}{\partial y} \\ \frac{\partial v}{\partial x} & \frac{\partial v}{\partial y} \end{bmatrix} \quad (3)$$

Note that in incompressible flows, $\text{tr}(M) \equiv 0$ at all times.

The instantaneous rate of deformation experienced by a small fluid element $\Delta \vec{x}$ is related to $M(t)$ by:

$$\frac{D}{Dt} \Delta \vec{x} = \Delta \frac{D \vec{x}}{Dt} = \Delta \vec{u} = M(t) \cdot \Delta \vec{x}$$

Observe that the symmetric component of $M(t)$ provides local strain and isotropic expansion, while the antisymmetric component of $M(t)$ provides local rotation (the rate of which equals half the vorticity). Thus, real eigenvalues of $M(t)$ represents physically the strain overcoming the rotation, leading to exponential deformation of the small fluid element *at that instant*. The instantaneous stretching rate $S(t)$ is properly the positive eigenvalue of $M(t)$, which is $[-\det(M)]^{1/2}$ in incompressible fluids.

To measure the *cumulative* stretching rate on a fluid element over a finite time interval $[t_i, t_f]$, one may imagine using the Lyapunov exponent λ computed over a finite-time interval^{[30],[31]}. It can be related to the instantaneous velocity gradient tensor $M(t)$ by:

$$\lambda(\theta; t_i, t_f) = \frac{1}{t_f - t_i} \int_{t_i}^{t_f} \hat{n}(\theta; t) \cdot M(t) \cdot \hat{n}(\theta; t) dt \quad (4)$$

Here, $\hat{n}(\theta; t)$ is a unit vector always parallel to an infinitesimal vector fluid element that is anchored at one end to the particle. It rotates with the local flow around that particle such that its orientation at time t_f is in direction θ . But there is a conceptual drawback to this measure: λ is a function of θ at finite times. Note that this dependence on initial orientation is still present in the two-vector approach of Pierrehumbert and Yang (1993)^[32].

In this paper, we measured the exponential deformation experienced by a fluid element *accumulated* over a finite time interval $[t_i, t_f]$ by the deformation exponent ξ . We define the deformation exponent ξ for a particle in a 2D incompressible flow as:

$$\xi(t_i, t_f) = \frac{1}{t_f - t_i} \ln \frac{P_f}{P_i} \quad (5)$$

where P_i is the length of a (sufficiently small) circular material contour centered on the particle at time t_i , and P_f is the length of the contour (deformed by advection) at time t_f .

From equations (4) and (6), the deformation exponent ξ is related to λ by:

$$e^{\xi(t_f - t_i)} = \frac{1}{2\pi} \int_0^{2\pi} \underbrace{e^{\lambda(t_f - t_i)}}_{\text{term A}} \underbrace{\sqrt{1 + (t_f - t_i)^2 \left(\frac{\partial \lambda}{\partial \theta}\right)^2}}_{\text{term B}} d\theta \quad (6)$$

Thus, the deformation exponent ξ of a particle measures the cumulative exponential stretching of small vector fluid elements (term A), averaged over all directions around the particle while weighted by the anisotropy of the stretching (term B). The anisotropy (term B) is unity when the growth is isotropic (which is incidentally impossible in a non-divergent fluid), and is proportional to the directional variation of stretch rates for highly anisotropic growth.

This physical interpretation of ξ explains why, in principle, it is a better finite-time Lagrangian measure of deformation than the finite-time Lyapunov exponent λ , namely that it is an average over all directions around a particle and it includes the effects of anisotropy. In the limit as t_f tends to ∞ , λ becomes independent of θ and approaches the (proper) Lyapunov exponent λ_∞ . Likewise, equation (6) shows that ξ also approaches λ_∞ . We suggest that as a measure of cumulative material deformation, ξ is the more appropriate conceptual generalization of λ_∞ to the finite-time context, as it is unique to each particle for a given $[t_i, t_f]$. Of course, in practice, the advantage is only significant for short time intervals where $(t_f - t_i) \lesssim 1/\xi$.

Unfortunately, the numerical computation of ξ is more expensive than that of λ , because one needs at least 3 points (we used 12 or more) to represent a contour around a particle, but only 1 point to represent a vector fluid element anchored on a particle. In our work, the calculation of ξ for a particle was a two-stage process. First, around the particle at time $t_0 \equiv \text{Day 10}$, we centered a small circular contour and advected it as a material contour forwards in time. At every time step, the multiplication factor $\Gamma(t, t + \delta t)$ in the contour length was calculated and then the contour was shrunk proportionately around the particle to restore its length to the

initial value. The deformation exponent $\xi(t_0, t_2)$ for the forward-time advection to $t_2 \equiv \text{Day } 17.5$ was calculated as :

$$\xi(t_0, t_2) = \frac{1}{t_2 - t_0} \sum_{t_0}^{t_2 - \delta t} \ln \Gamma(t, t + \delta t) \quad (7)$$

In the second stage, the same procedure was followed but with backward-time advection to $t_1 = \text{Day } 0$ to get $\xi(t_0, t_1)$ (a negative number). Finally, we take the weighted average $\bar{\xi}(t_1, t_2; t_0)$ as the deformation exponent $\xi(t_1, t_2)$ for the particle over $[t_1, t_2]$.

$$\xi(t_1, t_2) \approx \bar{\xi}(t_1, t_2; t_0) \equiv \frac{(t_1 - t_0) \xi(t_0, t_1) + (t_2 - t_0) \xi(t_0, t_2)}{t_2 - t_1}$$

This approximation is good owing to the large deformations involved (i.e. $\exp[\xi(t_0, t_k)(t_k - t_0)] \gg 1$, for $k = 1, 2$), because then, $\xi(t_1, t_2)$, $\xi(t_0, t_2)$ and $-\xi(t_0, t_1)$ all approximate to λ_∞ .

C. Time-Symmetric Node Advection Scheme

A numerical Lagrangian advection scheme is by definition an approximate way of integrating the equation $d\vec{x}/dt = \vec{u}$. Given a particle's position \vec{x}_n at time t_n , one possible approximation for the position \vec{x}_{n+1} at time $t_{n+1} \equiv t_n + \delta t$ is:

$$\begin{aligned} \vec{x}_{n+1} &= \vec{x}_n + \int_{t_n}^{t_{n+1}} \vec{u}(\vec{x}(t'), t') dt' \\ &\approx \vec{x}_n + \delta t \mathcal{F}(\vec{x}_n, t_n; \vec{x}_{n+1}, t_{n+1}) \end{aligned} \quad (8)$$

A time-symmetric advection scheme has to be implicit since it must depend on the past and the future equally. Moreover, \mathcal{F} must be invariant when the identities of (\vec{x}_n, t_n) and (\vec{x}_{n+1}, t_{n+1}) are interchanged. For our work, we used a 4th-order time-symmetric scheme where

$$\mathcal{F} = \frac{1}{2} [\mathcal{F}_{rk}(\vec{x}_n, t_n) + \mathcal{F}_{rk}(\vec{x}_{n+1}, t_{n+1})]$$

where \mathcal{F}_{rk} is the corresponding function to \mathcal{F} in the 4th order Runge-Kutta scheme.

However, equation (8) is not easily invertible to obtain an explicit form for \vec{x}_{n+1} , especially since the function \vec{u} comes from a non-trivial inversion of the PV distribution. Therefore, an iterative method initialized by the 4th order Runge-Kutta estimate was employed to approximate \vec{x}_{n+1} to a desired accuracy. We chose to iterate until two consecutive estimates differ by less than $10^{-3} \alpha^5 r_0$, where $\alpha \equiv f_0 \delta t / 2\pi = 0.1$. Note that the state of the flow \vec{u} must be known at both t_n and t_{n+1} at every step in forward or backward advection. So, the scheme is only applicable to diagnostic runs.

References

- [1] D. L. Hartmann, "Dynamical properties of the antarctic circumpolar vortex inferred from aircraft observations", in *Dynamics, transport, and photochemistry in the middle atmosphere of the Southern Hemisphere*, edited by A. O'Neill (Kluwer Academic Publishers, Boston, 1990).
- [2] D. W. Waugh, "Seasonal Variation of Isentropic Transport out of the Tropical Stratosphere", *J. Geophys. Res.* **101**, 4007 (1996).
- [3] P. C. Siegmund, P. F. J. van Velthoven and H. Kelder, "Cross-tropopause Transport in the Extratropical Northern Winter Hemisphere, diagnosed from High-resolution ECMWF Data", *Q. J. R. Meteorol. Soc.* **122**, 1921 (1996).
- [4] R. E. Newell, N. E. Newell, Y. Zhu, and C. Scott, "Tropospheric Rivers? - A Pilot Study", *Geophys. Res. Lett.* **12(24)**, 2401 (1992).
- [5] J. Duan, and S. Wiggins, "Fluid Exchange across a Meandering Jet with Quasiperiodic Variability", *J. Phy. Ocean.* **26**, 1176 (1996).
- [6] P. D. Miller, C. K. R. T. Jones, A. M. Rogerson and L. J. Pratt, "Quantifying transport in numerically generated velocity fields", *Physica D* **110**, 105 (1997).
- [7] A. C. Poje and G. Haller, "Geometry of Cross-Stream Mixing in a Double-Gyre Ocean Model", *J. Phy. Ocean.* **29**, 1649 (1999).
- [8] C. Coulliette and S. Wiggins, "Intergyre Transport in a Wind-Driven, Quasi-geostrophic Double Gyre: An Application of Lobe Dynamics", *Nonlinear Proc. in Geophys.*, submitted (1999).
- [9] J. M. Ottino, *The Kinematics of Mixing : Stretching, Chaos, and Transport* (Cambridge U. P., New York, 1989).
- [10] M. E. McIntyre, and T. N. Palmer, "Breaking planetary waves in the stratosphere", *Nature* **305**, 593 (1983).
- [11] D. W. Waugh, R. A. Plumb, R. J. Atkinson, M. R. Schoeberl, L. R. Lait, P. A. Newman, M. Loewenstein, D. W. Toohey, L. M. Avallone, C. R. Webster, and R. D. May, "Transport out of the Lower Stratospheric Artic Vortex by Rossby Wave Breaking", *J. Geophys. Res.* **9**, 1071 (1994).
- [12] R. A. Plumb, D. A. Waugh, R. J. Atkinson, P. A. Newman, L. R. Lait, M. R. Schoeberl, E. V. Browell, A. J. Simmons, and M. Loewenstein, "Intrusions into the Lower Stratospheric Artic Vortex during the Winter of 1991-1992", *J. Geophys. Res.* **9**, 1089 (1994).
- [13] S. P. Dahlberg, and K. P. Bowman, "Climatology of large-scale isentropic mixing in the arctic winter stratosphere from analyzed winds", *J. Geophys. Res.* **99**, 20585 (1994).

- [14] N. Nakamura, “Modified lagrangian mean diagnostics of the stratospheric polar vortices. Part I: formulation and analysis of GFDL SKYHI GCM”, J. Atmos. Sci. **52**(11), 2096 (1995).
- [15] A. H. Sobel, R. A. Plumb, and D. W. Waugh, “Methods of calculating transport across the polar vortex edge”, J. Atmos. Sci. **54**, 2241 (1997).
- [16] J. Thuburn, and V. Lagneau, “Eulerian mean, contour integral, and finite-amplitude wave activity diagnostics applied to a single-layer model of the winter stratosphere”, J. Atmos. Sci. **56**(5), 689 (1999).
- [17] L. M. Polvani, and R. A. Plumb, “Rossby wave breaking, microbreaking, filamentation and secondary vortex formation: the dynamics of a perturbed vortex”, J. Atmos. Sci. **49**(6), 462 (1992).
- [18] See web site “<http://gyre.cds.caltech.edu/bay.html>”.
- [19] K. Bowman, “Manifold Geometry, Mixing, and Mixing Barriers in the Stratosphere”, Nature, submitted (1999).
- [20] S. Wiggins, *Chaotic Transport in Dynamical Systems*. (Springer-Verlag, New York, 1992).
- [21] N. Malhotra, and S. Wiggins, “Geometric structures, lobe dynamics, and Lagrangian transport in flows with aperiodic time-dependence, with applications to Rossby wave flow”, J. Nonlinear Sci. **8**, 401 (1998).
- [22] G. Haller and A. C. Poje, “Finite Time Transport in Aperiodic Flows”, Physica D **119**, 352 (1998).
- [23] D. G. Dritschel, “Contour Surgery : A topological reconstruction scheme for extended integrations using contour dynamics”, J. Comput. Phys. **77**, 240 (1988).
- [24] M. N. Jukes, and M. E. McIntyre, “High-resolution one-layer model of breaking planetary waves in the stratosphere”, Nature **328**(6131), 590 (1987).
- [25] D. W. Waugh, and R. A. Plumb, “Contour Advection with Surgery: A Technique for Investigating Finescale Structure in Tracer Transport”, J. Atmos. Sci. **51**(4), 530 (1994).
- [26] M. Nakamura, and R. A. Plumb, “The effects of flow asymmetry on the direction of Rossby wave breaking”, J. Atmos. Sci. **51**(14), 2031 (1994).
- [27] P. Haynes and J. Anglade, “The Vertical-scale Cascade in Atmospheric Tracers due to Large-scale Differential Advection”, J. Atmos. Sci. **4**(9), 1121 (1997).
- [28] L. M. Polvani, G. R. Flierl, and N. J. Zabusky, “Filamentation of Unstable Vortex Structures via Separatrix Crossing: A Quantitative Estimate of Onset Time”, Phys. Fluids A **1**(2), 181 (1989).

- [29] G. K. Batchelor, *An Introduction to Fluid Dynamics* (Cambridge U. P., Cambridge, England, 1967), pp. 660.
- [30] A. Lichtenberg and M. Liberman, *Regular and Chaotic Motion* (Springer-Verlag, New York, 1983).
- [31] R. T. Pierrehumbert, “Large-scale horizontal mixing in planetary atmospheres”, *Phys. Fluids A* **3**(5), 1250 (1991).
- [32] R. T. Pierrehumbert and H. Yang, “Global Chaotic Mixing on Isentropic Surfaces”, *J. Atmos. Sci.* **50**, 2462 (1993).

Tables

Time	Lobe involved	Direction of transport	Amount transported = Lobe Area / r_0^2
Day 6.25	Li	Intrusion	0.72047 ± 0.00002
Day 10	Le	Extrusion	0.62397 ± 0.00009
Estimated transport in each direction / r_0^2			0.67 ± 0.05
Area of overlap O between lobes Li and Le / r_0^2			0.34 ± 0.07

Table I Measured transport of the periodic flow from Day 2.5 to Day 10 in Figure 4. (Note: $\Sigma = 0.3r_0$)

Time	Lobe involved	Direction of transport	Amount transported = Lobe Area / r_0^2
Day 12.5	Le#1	Extrusion	1.05 ± 0.03
Day 14.5	Li#1	Intrusion	0.0946 ± 0.0006
Day 16.5	Le#2	Extrusion	0.470 ± 0.001
Day 16.5	Li#2	Intrusion	0.0155 ± 0.0005
Total outward transport / r_0^2			1.52 ± 0.03
Total inward transport / r_0^2			0.110 ± 0.001

Table II Measured transport of the aperiodic flow from Day 0 to Day 17.5 in Figure 5. (Note: $\Sigma = 0.2r_0$)

Figures

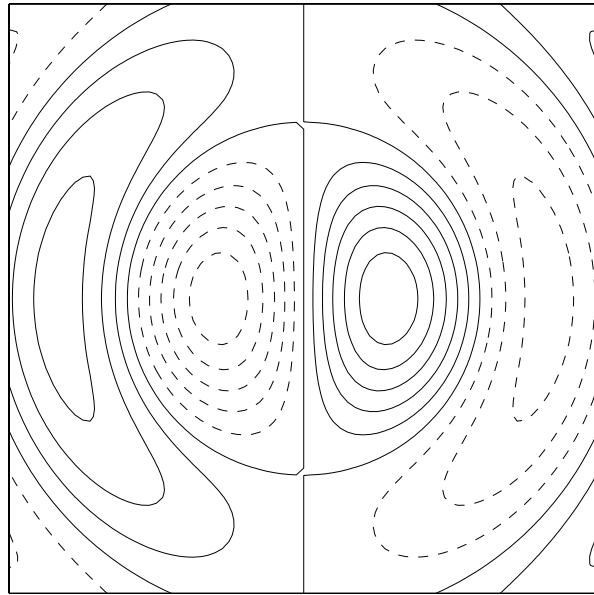


Figure 1: The spatial form of the bottom topographic forcing $J_1(\kappa r) \cos \theta$. Both axes are $[-4r_0, 4r_0]$. KEY: full lines are positive or zero, dashed lines are negative.

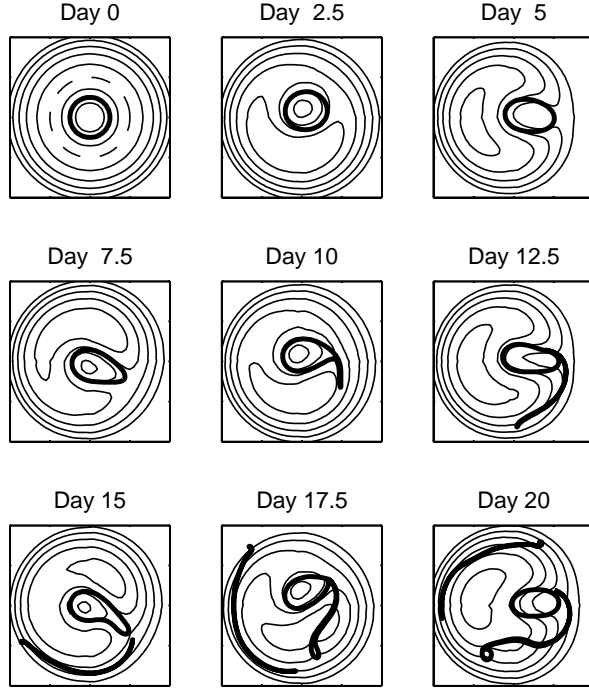


Figure 2: Evolution of the PV contour (thick) in the barotropic vortex model. The streamfunction (thin lines) is contoured at equal intervals. The flow is clockwise along the outermost streamline. Closed vortical flow (when present) is anticlockwise. The dashed line on Day 0 denotes the zero-wind line. Both axes are $[-4r_0, 4r_0]$.

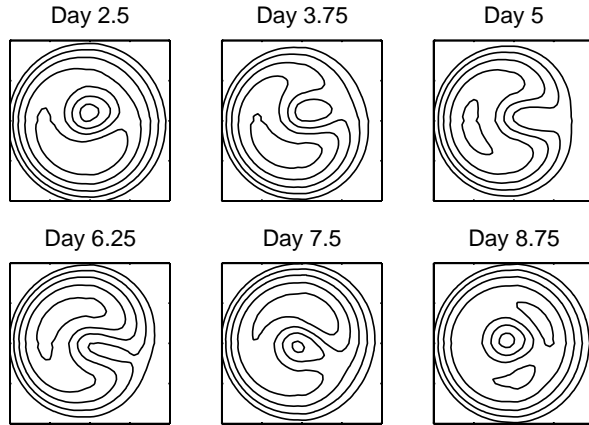


Figure 3: The equal-weighting composite kinematic flow constructed from the dynamically consistent flow over intervals $[\text{Day } 2.5, \text{Day } 10]$ and $[\text{Day } 10, \text{Day } 17.5]$. The streamfunction is contoured at equal intervals. Both axes are $[-4r_0, 4r_0]$.

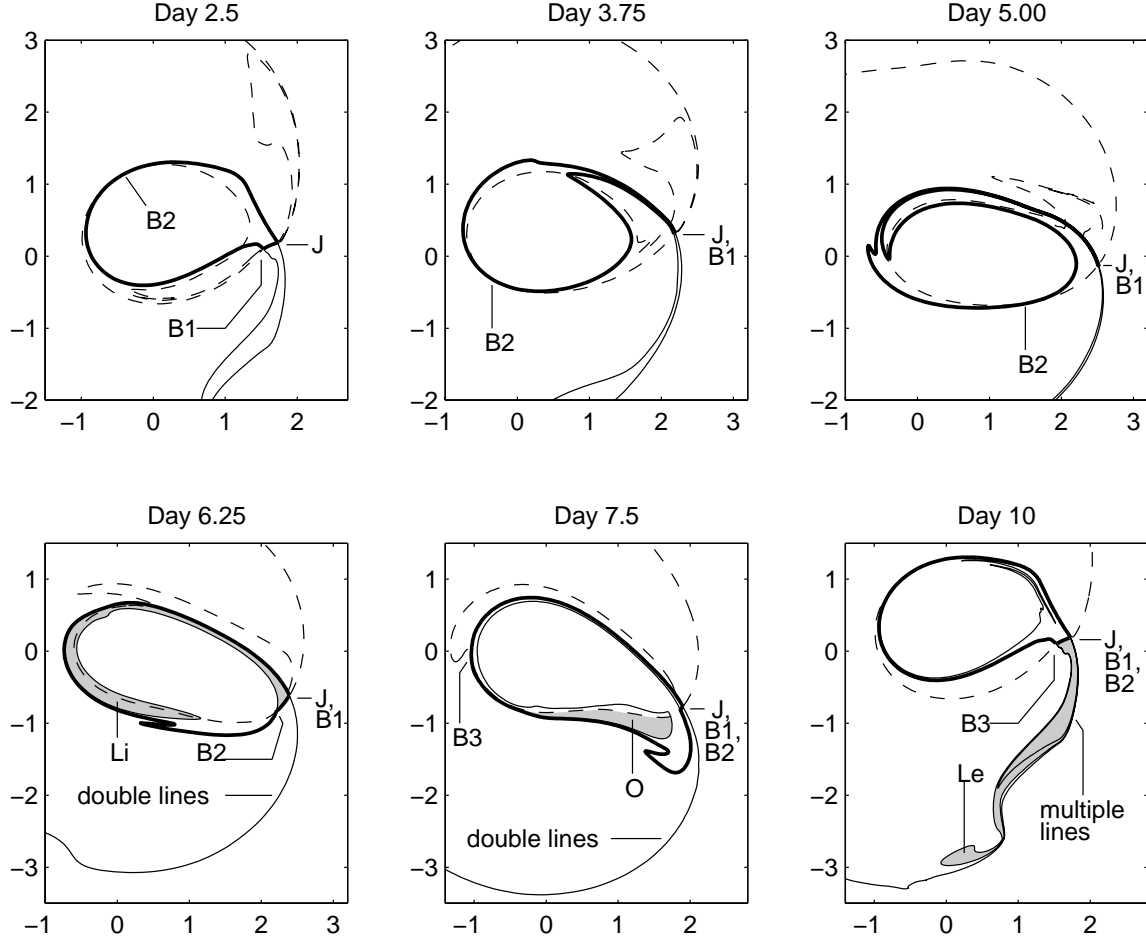


Figure 4: Lobe dynamics of the periodic kinematic flow. The thick full line is the lobe dynamical boundary. The PIP's are labelled by Bn ($n = 1, 2, 3$). The thin full and dashed lines are respectively the segments of the unstable (Wu) and stable (Ws) manifolds that do not lie on the lobe dynamical boundary. J is the hyperbolic trajectory. (Whenever, J and Bn 's are located very close together, they share a single line-pointer.) Intruding and extruding lobes are denoted by “Li” and “Le” respectively. Label “O” refers to the overlapping region between lobes Li and Le. For clarity, Li, O and Le are only shaded and labeled on Day 6.25, Day 7.5 and Day 10 respectively. Axes are labeled in units of r_0 .

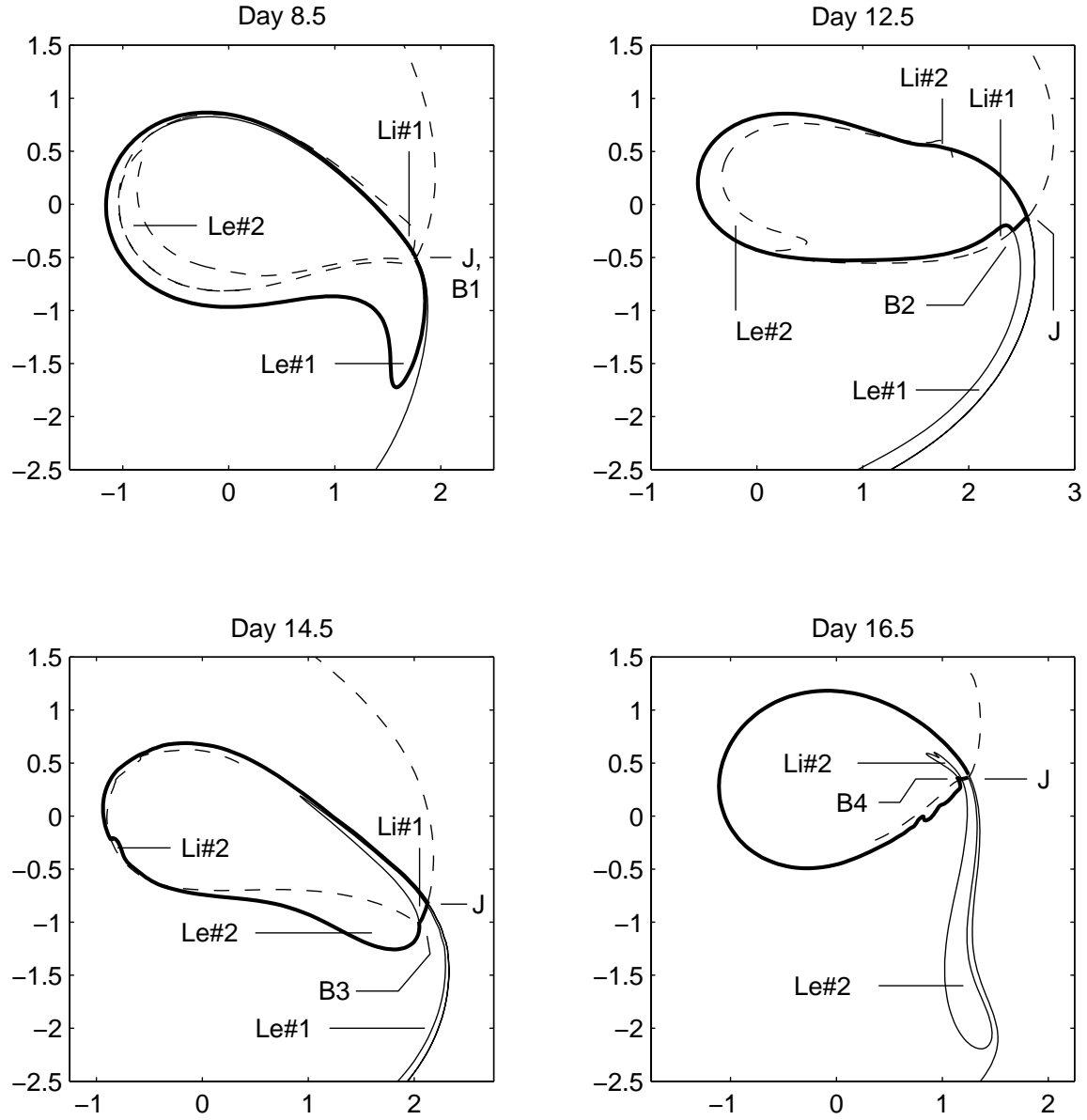


Figure 5: Lobe dynamics of the aperiodic dynamically consistent flow from Day 0 to Day 17.5, at irregular time intervals. The same graphical representation as in Figure 4 is used. Intruding and extruding lobes are numbered independently.

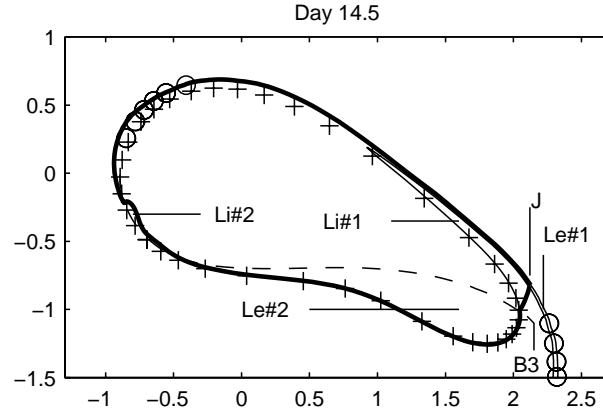


Figure 6: The stable and unstable manifolds, and the hyperbolic trajectory on Day 14.5. Crosses denote the perimeter of the PV vortex. Circles denote thin high-PV filaments. Otherwise, the same graphical representation as in Figure 4 is used.

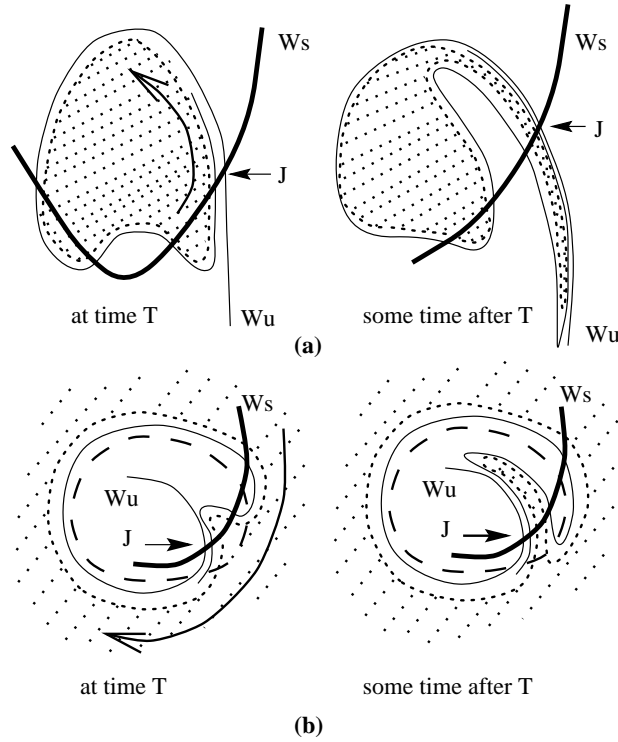


Figure 7: Schematic diagrams of (a) a cyclonic flow with an exterior hyperbolic trajectory; (b) an anticyclonic flow with an interior hyperbolic trajectory. KEY: thick solid line (W_s) = stable manifold; thin solid line (W_u) = unstable manifold; J = hyperbolic trajectory; dashed line = critical line; shaded mass = high PV in (a) and low PV in (b).

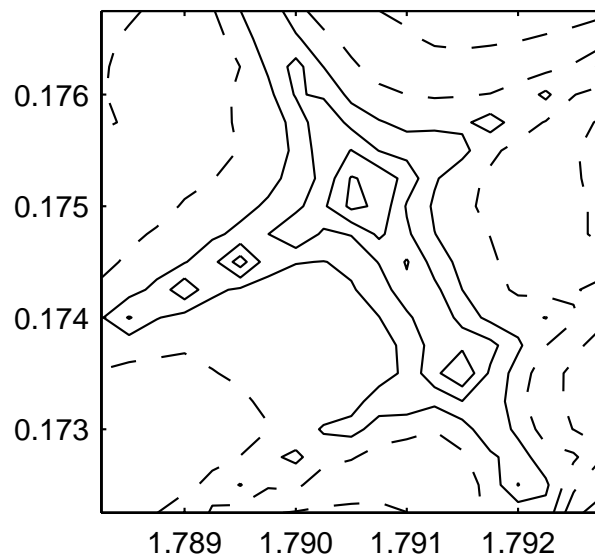


Figure 8: Distribution of the deformation exponent ξ over a subset of \mathcal{A} . The cross-like formations are reminiscent of homoclinic tangles around a hyperbolic trajectory. (See Appendix A and B for more details.) KEY: contour interval is 0.05/day; solid lines are 0.85/day or greater; dashed lines are 0.80/day or smaller. Axes are labelled in units of r_0 .